# Geochemical and Mineralogical Characterization of Sangiran Mud Vulcano: Insights into Rare Earth Element (REE) Enrichment

(Pencirian Geokimia dan Mineralogi Gunung Berapi Lumpur Sangiran: Pandangan terhadap Pengayaan Unsur Nadir Bumi (REE))

CAHYO AJI HAPSORO<sup>1,\*</sup>, KHARISMA ASMARANI BUDIONO<sup>1</sup>, MOCHAMAD KHOIRUL RIFAI<sup>1</sup>, ALPAN IBRAHIM<sup>1</sup>, MARIYANTO MARIYANTO<sup>2,6</sup>, ELEONORA AGUSTINE<sup>3</sup>, RINA DWI INDRIANA<sup>4</sup> & MIMIN IRYANTI<sup>5</sup>

<sup>1</sup>Department of Physics, Faculty of Mathematics and Natural Sciences, State University of Malang, Jl. Semarang 5, Malang, 65145, Indonesia

<sup>2</sup>Department of Geophysical Engineering, Faculty of Civil, Planning, and Geo-Engineering, Institut Teknologi Sepuluh Nopember, Surabaya, 60111, Indonesia

<sup>3</sup>Department of Geophysics, Faculty of Mathematics and Natural Science, Padjajaran University, Jl. Ir. Soekarno KM 21, Sumedang, 45363, Indonesia

<sup>4</sup>Department of Physics, Faculty of Science and Mathematics, Diponegoro University, Jl. Prof. Soedarto, SH, Semarang, 1269, Indonesia

<sup>5</sup>Department of Educational Physics, Faculty of Education of Mathematics and Natural Science, Indonesia University of Education, Jl. Dr. Setiabudhi 229, Bandung, 40154, Indonesia

<sup>6</sup>Faculty of Mining and Petroleum Engineering, Institut Teknologi Bandung, Jl. Ganesha 10, Bandung, 40132, Indonesia

Received: 20 January 2025/Accepted: 11 August 2025

## ABSTRACT

The Sangiran Mud Volcano (SMV), an inactive mud volcano located in Central Java, Indonesia, exhibits a unique geological framework with promising potential for Rare-Earth Element (REE) mineralization. This study explores the geochemical properties and REE mineral content of SMV through comprehensive analytical methods, including magnetic susceptibility measurements for magnetic property analysis, X-Ray Fluorescence (XRF) for quantitative elemental analysis, X-Ray Diffraction (XRD) X'Pert PRO PANalytical plays a role in identifying the crystalline phases of REE-related minerals, Scanning Electron Microscopy-Energy Dispersive X-Ray Energy Dispersive Spectroscopy (SEM-EDS) Hitachi Flexsem 1000 provides microscopic characterization of morphology and elemental composition, and Inductively Coupled Plasma-Optical Emission Spectroscopy (ICP-OES) is used to determine REE concentrations with high precision. The findings showed that SMV samples mostly consist of hematite and cerium, with average concentrations of 83.16% and 16.83%, respectively. Further geochemical analysis identified significant concentrations of REEs, particularly lanthanum (La) and cerium (Ce), with La showing the highest average concentration at 44.39 ppm, followed by Ce at 37.96 ppm. Additionally, XRF analysis showed that the oxide composition in the samples was dominated by SiO<sub>2</sub> (55.36%), followed by Fe<sub>2</sub>O<sub>3</sub> (17.18%), Al<sub>2</sub>O<sub>2</sub> (11.11%), CaO (15.73%), TiO<sub>2</sub> (1.02%), K<sub>2</sub>O (0.8%), and ZrO<sub>2</sub> (0.048%). XRD analysis showed the highest potential REE content in samples T1 and T7, with silicon iron cerium deuteride concentrations of 19.8% and 19.4%, respectively. SEM-EDS spectra showed that carbon (C) and oxygen (O) are the main elements, while lower concentrations of Al, Si, Fe, K, and Ca were observed, and trace elements, including Mg and Na, were also detected in small amounts, and ICP-OES analysis detected other REEs, including dysprosium (Dy), europium (Eu), gadolinium (Gd), holmium (Ho), neodymium (Nd), praseodymium (Pr), samarium (Sm), terbium (Tb), yttrium (Y), and scandium (Sc). This decision highlights the potential for REE mineralization in the SMV. Further exploration and characterization of this region could enhance understanding of REE enrichment processes in mud volcano systems and have significant implications for future resource development.

Keywords: Geochemical analysis; hematite and cerium; mineralization potential; Rare Earth Elements (REE); Sangiran Mud Volcano (SMV)

## ABSTRAK

Gunung Berapi Lumpur Sangiran (SMV), gunung berapi lumpur tidak aktif yang terletak di Jawa Tengah, Indonesia, mempamerkan rangka kerja geologi yang tersendiri dengan potensi untuk mineralisasi Unsur Nadir Bumi (REE). Penyelidikan ini meneroka sifat geokimia dan kandungan mineral REE SMV melalui kaedah analisis yang komprehensif,

termasuk pengukuran kerentanan magnet digunakan untuk analisis sifat magnetik material, Pendaflour Sinar-X (XRF) digunakan untuk analisis unsur kuantitatif, Belauan Sinar-X (XRD) X'Pert PRO PANalytical memainkan peranan dalam mengenal pasti fasa kristal mineral berkaitan REE, Mikroskopi Elektron Imbasan-Serakan Tenaga Sinar-x Spektroskopi Serakan Tenaga (SEM-EDS) Hitachi Flexsem 1000 menyediakan pencirian mikroskopik morfologi dan komposisi unsur dan Spektrometri Pemancaran Plasma-Optik Berganding Secara Induktif digunakan untuk menentukan kepekatan REE dengan ketepatan tinggi. Penemuan menunjukkan bahawa sampel SMV kebanyakannya terdiri daripada hematit dan serium dengan kepekatan purata masing-masing 83.16% dan 16.83%. Analisis geokimia selanjutnya mengenal pasti kepekatan ketara REE, khususnya lanthanum (La) dan serium (Ce) dengan La menunjukkan kepekatan purata tertinggi pada 44.39 ppm diikuti oleh Ce pada 37.96 ppm. Selain itu, analisis XRF menunjukkan sebatian oksida dalam sampel didominasi oleh  $SiO_2$  (55.36%), diikuti oleh  $Fe_2O_3$  (17.18%),  $Al_2O_3$  (11.11%), CaO (15.73%),  $TiO_2$  (1.02%),  $K_2O$  (0.8%) dan  $ZrO_3$  (11.11%), CaO (15.73%), CaO (15.73%), CaO (10.2%), CaO (1 (0.048%), analisis XRD menunjukkan kandungan REE berpotensi tertinggi dalam sampel T1 dan T7 dengan kepekatan deuteride silikon besi serium masing-masing sebanyak 19.8% dan 19.4%, spektrum SEM-EDS mendedahkan bahawa karbon (C) dan oksigen (O) adalah unsur utama, manakala kepekatan Al, Si, Fe, K dan Ca yang lebih rendah diperhatikan sedangkan unsur kecil, termasuk Mg dan Na juga dikesan dalam jumlah surih dan analisis ICP-OES mengesan REE lain, termasuk dysprosium (Dy), europium (Eu), gadolinium (Gd), holmium (Ho), neodymium (Nd), praseodymium (Pr), samarium (Sm), terbium (Tb), yttrium (Y) dan skandium (Sc). Keputusan ini menggariskan potensi untuk mineralisasi REE dalam SMV. Penerokaan dan pencirian yang lebih terperinci bagi rantau ini boleh meningkatkan pemahaman proses pengayaan REE dalam sistem gunung berapi lumpur dan mempunyai implikasi yang ketara untuk pembangunan sumber masa hadapan.

Kata kunci: Analisis geokimia; Gunung Berapi Lumpur Sangiran (SMV); hematit dan serium; potensi mineralisasi; Unsur Nadi Bumi (REE)

#### INTRODUCTION

The formation of mud volcanoes is primarily influenced by young magmatic activity, intensive tectonic compression, and rapid sedimentation processes (Mazzini & Etiope 2017; Novianto et al. 2022; Samankassou et al. 2018). In Indonesia, mud volcanoes generally result from eruptions of debris and clay materials (Isnaniawardhani, Muhamadsyah & Sudrajat 2018). A significant number of mud volcanoes are located in Indonesia, particularly on Java Island. Some are classified as active volcanoes, while others are inferred based on the characteristics of their rock deposits (Bronto, Asmoro & Efendi 2017; Hidayat & Novianto 2020). On Java Island, the distribution of mud volcanoes aligns in a linear formation, corresponding to the active mud volcano belt, which extends from Purwodadi through Cepu, Bojonegoro, and Porong (Indriana et al. 2023).

This research was conducted at the Sangiran Mud Volcano (SMV), one of the mud volcanoes located in Central Java. SMV is part of the Boyolali mud volcano complex, an inactive and ancient mud volcano system. Within this complex, several other mud volcanoes, including Jatikuwung, Tengklik Lake, and Gununglondo have been identified. These mud volcanoes exhibit various geological features, such as diapirs, mud balls, sill-like volcanic deposits, and hardened mud structures (Bronto, Asmoro & Efendi 2017; Hidayat & Novianto 2020; Indriana et al. 2023). The dome at the SMV was formed by eruptions of mud and gas from underground layers composed of volcanic rocks and sedimentary deposits (Hapsoro et al. 2023).

Mud volcanoes typically emit fluids containing hydrocarbons and gases, such as methane, carbon dioxide,

and nitrogen. The mechanism of fluid and material release in mud volcanoes is analogous to that of conventional volcanic eruptions but differs in terms of pressure, temperature (which is lower in mud volcanoes), and the nature of the ejected materials (Galos et al. 2021; Indriana et al. 2024; Maestrelli, Bonini & Sani 2019; Mauri et al. 2018a, 2018b; Mazzini et al. 2023). Notably, Rare-Earth Elements (REEs) have been identified as significant minerals within the residual mud material expelled during mud volcano eruptions. REE is an important commodity that has been recognized by national and international institutions because it is included in the critical and strategic metal elements (Galos et al. 2021). Minerals such as REE play a role in renewable energy sources (clean energy), the national defense industry, and high-tech electronic devices (Blengini et al. 2017).

Advanced materials have become essential components in various high-tech industries, and the availability and development of these materials are increasingly seen as indicators of a country's industrial progress. In this context, Indonesia needs to invest in research on advanced materials to support the growth of its domestic industrial capabilities. The development of the industrial sector offers various strategic benefits, including: (a) enhancing the value and competitiveness of Indonesia's natural resources, (b) reducing dependence on imported products, (c) increasing the use of local materials, (d) creating job opportunities, and (e) increasing state revenue through taxes. Advanced materials research aims to develop strategic control over critical materials that underpin technological innovation, with a particular focus on REEs, permanent magnet materials, solid-state battery materials, and silicon-based materials.

Rare Earth Elements refer to a group of 17 chemically similar metals, consisting of 15 lanthanides plus scandium (Sc) and yttrium (Y), which share similar chemical properties. Despite being labeled 'rare', these elements are relatively abundant in the Earth's crust. The main challenge lies in identifying reserves with economically viable concentrations. REEs are crucial for various high-tech applications, including permanent magnets in renewable energy technologies such as wind turbines and electric vehicles (e.g., neodymium, praseodymium, and dysprosium), essential for everyday electronics from smartphones to LEDs, vital in advanced national defense systems, and playing a key role in catalytic converters (e.g., cerium) and various chemical processes.

In nature, REEs are not found in their elemental form but are bound within specific mineral matrices. Primary minerals containing REEs include bastnaesite, monazite, xenotime, loparite, and ion-adsorption clays, while secondary sources include allanite and various geological associations such as carbonatites, alkaline rocks, placer deposits, hydrothermal systems, and mud volcanoes. For example, in Sangiran, Central Java, Indonesia, REEs can be concentrated in mud materials extracted from deep sediment layers. Previous studies by Galos et al. (2021) reported significant REE concentrations in mud volcanoes, particularly those associated with hydrocarbon systems or intense tectonic activity.

Globally, REE concentrations in mud volcanoes vary widely, influenced by geological settings, hydrothermal processes, and source magma composition. For example, mud from the Taupo Volcanic Zone in New Zealand contains up to 200 ppm of lanthanum (La) and cerium (Ce), while acidic volcanic rocks at Ijen Crater, Indonesia, produce mud with high concentrations of yttrium (Y) and neodymium (Nd). However, existing data remain fragmented, highlighting the need for more comprehensive mapping and systematic analysis of mineral associations, fluid pH, and hydrothermal alteration processes. Such studies are crucial for optimizing REE exploration and extraction strategies, particularly in active volcanic regions like Indonesia, Iceland, and Japan.

Current research on SMV is still limited, primarily focusing on morphological characteristics. This study aims to investigate the REE potential of Sangiran Volcanic Mud through an integrated geochemical and mineralogical approach, utilizing analytical techniques including X-Ray Fluorescence (XRF), X-Ray Diffraction (XRD), Inductively Coupled Plasma-Optical Emission Spectroscopy (ICP-OES), Vibrating Sample Magnetometry (VSM), and Scanning Electron Microscopy combined with Energy Dispersive X-Ray Spectroscopy (SEM-EDS).

Research conducted at the SMV employs ICP-OES geochemical analysis to characterize REE in the Sangiran mud. This study is pioneering in its application of ICP-OES for REE characterization in this context. Previous studies (Hapsoro et al. 2023), utilized XRF to identify sediment

formation and elemental composition in Sangiran mud, showing that the samples are predominantly composed of Si, Fe, Al, Ca, Cl, Ti, and K, with Si and Fe being the most abundant elements. The objective of this study was to investigate the presence of REE in the SMV using a combination of rock magnetism and geochemical methods. Magnetic properties are assessed through measurements of magnetic susceptibility, which helps determine the magnetic characteristics and identify the presence of metallic elements in the samples.

To measure REE concentrations, a comprehensive suite of geochemical characterization techniques is employed, including XRF, XRD, ICP-OES, VSM, and SEM-EDS. The data obtained from these analyses are valuable for advancing the exploration and exploitation of REE in the Sangiran dome area. Large-scale exploration could capitalize on REE as critical raw materials for the electronics industry, offering significant benefits to the broader community.

## MATERIALS AND METHODS

The Sangiran Mud Volcano (SMV) is located in the Sangiran dome area, Central Java Province, Indonesia, at geographic coordinates 7°27'5" S and 110°50'15.36" E, as shown in Figure 1. This study involved collecting mud samples from two distinct locations within the Sangiran sediment area, Sragen. The sampling sites, identified by methane gas emissions in the form of saltwater bubbles, were located at 7°27'26.26" S, 110°50'04.05" E for the northern site and 7°27'10.28" S, 110°50'19.34" E for the southern site, as shown in Figure 2. The collected mud samples were labeled according to their respective locations and stored in airtight containers for laboratory analysis. There are seven mud samples from seven different sampling points.

Magnetic susceptibility measurements were conducted using the Bartington MS2B sensor to evaluate pollution levels. This method involves comparing magnetic susceptibility values at two frequencies: low-frequency magnetic susceptibility ( $\chi_{Lf}$ ) and high-frequency magnetic susceptibility ( $\chi_{Hf}$ ). The frequency-dependent magnetic susceptibility factor ( $\chi_{fd}$ ) was calculated to assess the presence of very fine magnetic minerals, such as superparamagnetic particles, which are often associated with pollutant sources. High  $\chi_{fd}$  values (>5%) indicate a significant potential for contamination, typically linked to magnetic particles from anthropogenic pollution sources.

XRD (X-Ray Diffraction) is a non-destructive and highly reliable method for identifying phases and characterizing the crystal structure of materials. The diffraction pattern generated by XRD, often referred to as a material's fingerprint, is highly sensitive to variations in composition, grain size, and internal stress within the sample. Due to its precision, XRD is widely applied across various fields, including materials science and geology. In this study, XRD analysis was conducted using XRD X'Pert PRO PANalytical. Seven samples, labeled T1, T2, T3, T4, T5, T6, and T7, were analyzed.

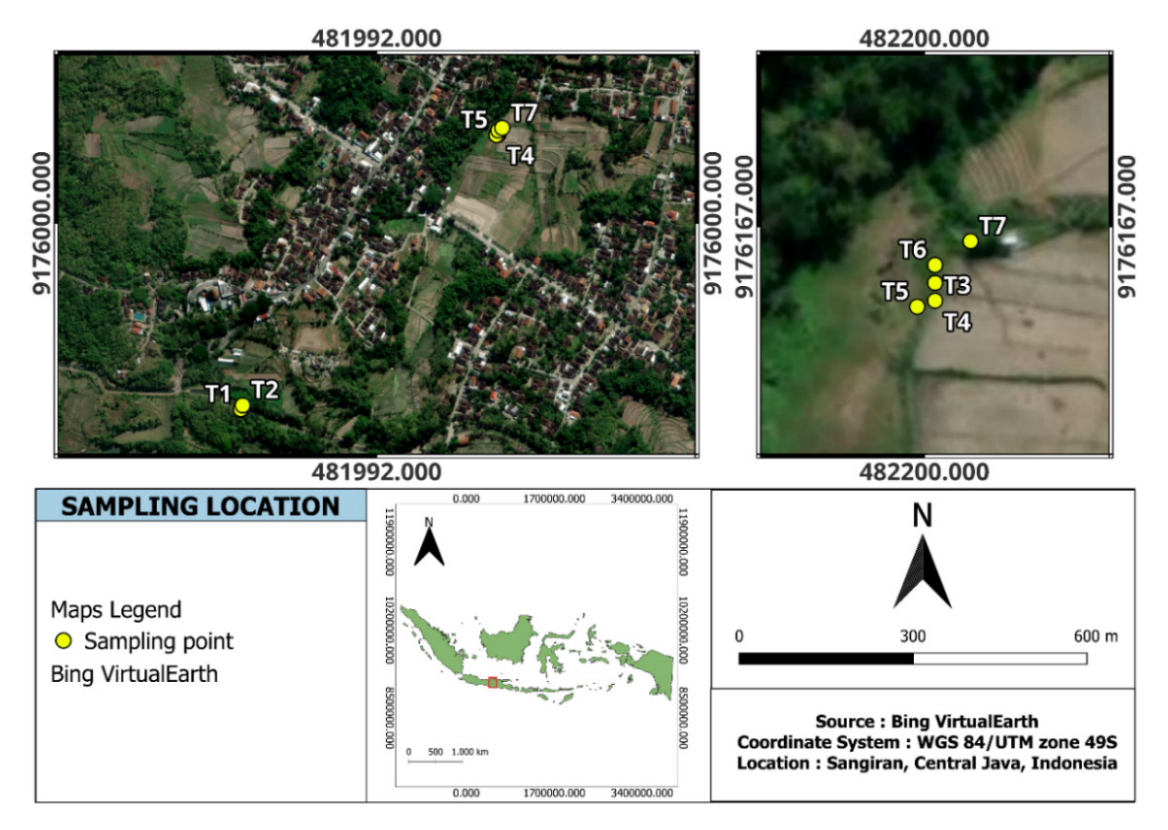


FIGURE 1. Sangiran Mud Volcano (SMV) location and sampling point

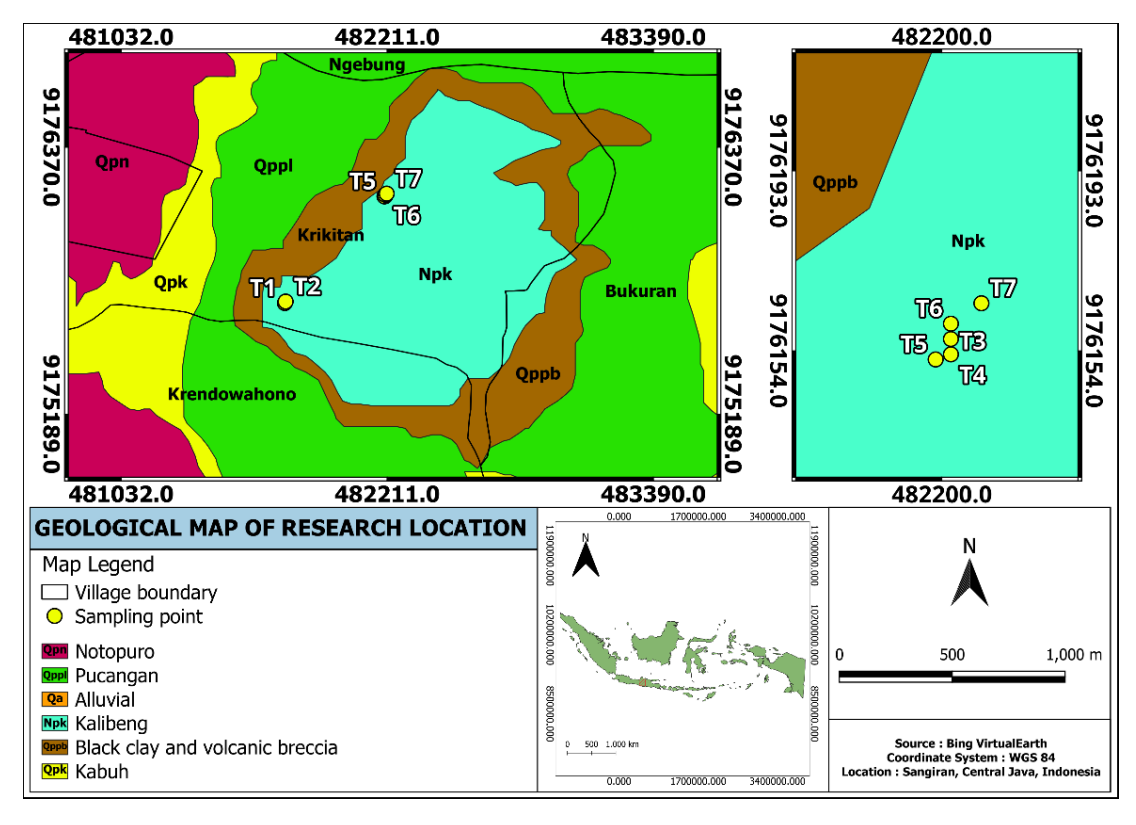


FIGURE 2. Geology map of Sangiran Mud Volcano (SMV) and sampling point

SEM (Scanning Electron Microscopy) operates by scanning a sample's surface with a focused high-energy electron beam. This electron beam interacts with the sample's atoms, producing several signals, such as secondary electrons, backscattered electrons, and characteristic X-rays. These signals are detected and processed to generate detailed images of the sample's surface. By integrating an EDS (Energy Dispersive Spectroscopy) detector, SEM can perform quantitative elemental analysis based on the energy of the emitted X-rays. The SEM-EDS technique enables simultaneous examination of a sample's morphology, topography, and chemical composition for material characterization. SEM-EDS analysis was performed using Hitachi Flexsem 1000.

**ICP-OES** Research REE frequently employs (Inductively Coupled Plasma Optical Spectrometry), a technique renowned for its precision in identifying and quantifying multiple REE in a sample. ICP-OES operates by exciting sample atoms within a high-temperature argon plasma, subsequently measuring the intensity of the emitted radiation, which correlates with elemental concentrations. This method's capability to deliver accurate and comprehensive quantitative data makes it indispensable across various disciplines, including geochemistry, environmental science, and materials research. ICP-OES analysis was performed using the ICP-EOS 8300 PERKINELMER. The ICP OES test uses a standard stock solution with a concentration of 1000 ppm. The working range is low in the standard series of 0.05-2 ppm. The digestion process is carried out with three acids, namely nitric acid, sulfuric acid and hydrochloric acid.

Chemical analysis of REE in geological, industrial, and environmental samples is vital for applications such as geochemical exploration, mining, resource extraction, and environmental monitoring. REE are positioned in the periodic table with atomic numbers ranging from 57 to 71, and are further classified into Light Rare Earth Elements (LREE) from <sup>57</sup>La to <sup>63</sup>Eu and Heavy Rare Earth Elements (HREE) from <sup>64</sup>Gd to <sup>71</sup>Lu (Table 1), with yttrium (Y) often included in the HREE group due to its similar chemical properties (Dushyantha et al. 2020; Gwenzi et al. 2018).

The conservative geochemical properties of REE make them valuable indicators for reconstructing the geological history of a system. To determine REE concentrations, analyses were conducted using ICP-OES with a PerkinElmer Optima 8300 spectrometer at the National Research and Innovation Agency (Badan Riset dan Inovasi Nasional – BRIN, Indonesia) facility. The REE concentration data obtained were then utilized to interpret the geochemical processes that influenced the formation and evolution of the analyzed samples.

Multivariate analysis, a statistical approach for simultaneously examining multiple variables, is commonly applied to study complex datasets. One widely used method is PCA (Principal Component Analysis), which reduces data dimensionality by identifying principal components -

uncorrelated linear combinations of the original variables. These components are selected based on their ability to explain the maximum variance in the dataset (Kumar et al. 2020). In PCA, an eigenvalue greater than one serves as a key criterion for selecting components for further analysis (Leventeli & Yalcin 2021).

When combined with Pearson correlation analysis, PCA enables the identification of potential sources of REE in samples and facilitates the classification of elements based on their geochemical affinities. This integrated approach provides deeper insights into the relationships between REE and the geological processes responsible for the formation of the samples (El-Taher et al. 2019; Iwamori et al. 2020).

#### RESULTS AND DISCUSSION

Magnetic susceptibility measurements of the Sangiran Mud Volcanoes (SMV) samples yielded values for low-frequency susceptibility ( $\chi_{\rm Lf}$ ), high-frequency susceptibility ( $\chi_{\rm Hf}$ ), and frequency-dependent susceptibility ( $\chi_{\rm fd}$ ). The  $\chi_{\rm Lf}$  values ranged from  $31.6 \times 10^{-8}$  to  $897 \times 10^{-8}$  m³/kg, with an average of  $367.06 \times 10^{-8}$  m³/kg. The  $\chi_{\rm Hf}$  values ranged from  $31.6 \times 10^{-8}$  to  $891 \times 10^{-8}$  m³/kg, with an average of  $364.4 \times 10^{-8}$  m³/kg. While  $\chi_{\rm fd}$  values ranged from 0% to 1.57%, with an average of 0.72%, as shown in Table 2.

According to Dearing et al. (1996) classification, the low  $\chi_{\rm fd}$  values (<2%) indicate an absence of superparamagnetic grains in the samples. The magnetic properties of these sediments are likely influenced by the presence of metal elements, particularly iron (Fe) and magnesium (Mg). Further studies are recommended to quantify these elements and establish their correlation with the observed magnetic susceptibility values.

To complement the magnetic susceptibility data, XRF (X-Ray Fluorescence) analysis was conducted using a Thermoscientific ARL QUANT' X ED' XRF Analyzer to determine the chemical composition of the sediment samples. The primary elements identified included Si, Fe, Al, Ca, Cl, Ti, and K. In specific sampling points, the dominant elements varied: in T1, Si (29.48%) and Fe (13.66%) were prevalent; in T2, Si (27.73%) and Fe (10.26%); in T6, Si (23.13%) and Fe (12.63%); and in T7, Si (24.95%) and Fe (12.01%). Conversely, samples from T3, T4, and T5, collected from adjacent locations, were dominated by Si and Ca, with respective values of Si (23.49%, 23.45%, and 23.47%) and Ca (12.44%, 13.45%, and 13.75%). On average, the oxide compounds in the samples were dominated by SiO<sub>2</sub> (55.36%), followed by Fe<sub>2</sub>O<sub>3</sub> (17.18%), Al<sub>2</sub>O<sub>3</sub> (11.11%), CaO (15.73%), TiO<sub>3</sub> (1.02%), K<sub>2</sub>O (0.8%), and ZrO<sub>2</sub> (0.048%), as shown in Table 3.

The XRD (X-Ray Diffraction) analysis was conducted to determine the crystalline structure of the Sangiran sediment samples, which were collected as mud from various locations. The list of ICCD numbers for XRD tests includes quartz (ICDD number 96-901-0147), Al,H<sub>4</sub>O<sub>o</sub>Si,

TABLE 1. Classification and magnetic properties of REE

| LREE              | Magnetic properties | HREE            | Magnetic properties |
|-------------------|---------------------|-----------------|---------------------|
| Lanthanum (La)    | Non-magnetic        | Europium (Eu)   | Magnetic            |
| Cerium (Ce)       | Magnetic            | Gadolinium (Gd) | Magnetic            |
| Praseodymium (Pr) | Magnetic            | Terbium (Tb)    | Magnetic            |
| Neodymium (Nd)    | Magnetic            | Dysprosium (Dy) | Magnetic            |
| Samarium (Sm)     | Magnetic            | Holmium (Ho)    | Magnetic            |
|                   |                     | Erbium (Er)     | Magnetic            |
|                   |                     | Thulium (Tm)    | Magnetic            |
|                   |                     | Ytterbium (Yb)  | Non-magnetic        |
|                   |                     | Lutetium (Lu)   | Non-magnetic        |
|                   |                     | Yttrium (Y)     | Non-magnetic        |

TABLE 2. Susceptibility magnetic of the SMV samples

| Sample code | $\chi_{\rm Lf}(10^{-8} {\rm m}^3/{\rm kg})$ | $\chi_{\rm Hf}(10^{-8}~{\rm m}^3/{\rm kg})$ | $\chi_{\rm fd}(\%)$ |
|-------------|---------------------------------------------|---------------------------------------------|---------------------|
| T1          | 465.5                                       | 464.2                                       | 0.28                |
| T2          | 31.6                                        | 31.6                                        | 0.00                |
| Т3          | 375.2                                       | 373.9                                       | 0.45                |
| T4          | 235.5                                       | 232.0                                       | 1.49                |
| T5          | 140.4                                       | 138.2                                       | 1.57                |
| Т6          | 424.2                                       | 421.8                                       | 0.57                |
| T7          | 897.0                                       | 891.1                                       | 0.66                |

TABLE 3. XRF element and compound concentration of the Sangiran mud samples

| Samples | Oxides               |                   |                   |         |                      |                      |               |  |  |
|---------|----------------------|-------------------|-------------------|---------|----------------------|----------------------|---------------|--|--|
| Samples | SiO <sub>2</sub> (%) | $Fe_{2}O_{3}$ (%) | $Al_{2}O_{3}$ (%) | CaO (%) | TiO <sub>2</sub> (%) | K <sub>2</sub> O (%) | $ZrO_{2}$ (%) |  |  |
| T1      | 63.07                | 19.54             | 7.61              | 4.12    | 1.41                 | 1.20                 | 0.06          |  |  |
| T2      | 59.31                | 14.68             | 7.08              | 3.7     | 1.34                 | 2.09                 | 0.069         |  |  |
| Т3      | 50.25                | 15.78             | 9.13              | 17.4    | 0.97                 | 1.00                 | 0.055         |  |  |
| T4      | 50.18                | 16.25             | 7.01              | 18.81   | 1.05                 | 0.90                 | 0.05          |  |  |
| T5      | 50.21                | 14.92             | 7.74              | 19.23   | 1.05                 | 0.92                 | 0.048         |  |  |
| T6      | 49.48                | 18.06             | 4.71              | 13.94   | 1.62                 | 0.80                 | 0.05          |  |  |
| T7      | 53.36                | 17.18             | 11.11             | 15.73   | 1.02                 | 0.80                 | 0.04          |  |  |
| Average | 55.36                | 17.18             | 11.11             | 15.73   | 1.02                 | 0.80                 | 0.048         |  |  |

(ICDD number 96-155-0599) and CCaO $_3$  (ICDD number 96-900-9669). Sample T1, taken from the south Sangiran area, exhibited a composition of 80.2% hematite-proto (Fe $_{1.9}$ H $_{0.06}$ O $_3$ ) and 19.8% cerium iron silicon deuteride (Ce $_2$ D $_{2.78}$ Fe $_{15}$ Si $_2$ ). The density of hematite-proto in T1 was measured at 5.084 g/cc, while cerium iron silicon deuteride had a density of 7.413 g/cc, as shown in Figure 3.

Samples T4 and T7, obtained from the north Sangiran region, displayed similar crystalline components but with variations in concentrations. In T4, hematite-proto (Fe $_{1.76}$ H $_{0.06}$ O $_3$ ) constituted 88.7% of the sample, and cerium iron silicon deuteride (Ce $_2$ D $_{2.78}$ Fe $_{15}$ Si $_2$ ) accounted for 11.3%, with densities of 4.889 g/cc and 7.413 g/cc, respectively, as shown in Figure 4. T7 contained 80.6%

hematite-proto (Fe<sub>1.9</sub>H<sub>0.06</sub>O<sub>3</sub>) with a density of 5.121 g/cc and 19.4% cerium iron silicon deuteride (Ce<sub>2</sub>D<sub>0.79</sub>Fe<sub>14</sub>Si<sub>3</sub>) with a density of 7.354 g/cc (Figure 5). These density variations align with the typical range for hematite, which spans from 4.2 to 5.3 g/cc (Courtney-Davies et al. 2019). The density of cerium iron silicon deuteride reflects its complex composition, with individual elements exhibiting densities of 6.69 g/cc for cerium (Ce), 7.87 g/cc for iron (Fe), and 2.33 g/cc for silicon (Si) (Casadei et al. 2012).

The concentrations of hematite-proto and cerium iron silicon deuteride across samples are summarized in Table 4. Hematite, the dominant component, is a primary iron ore mineral with the chemical formula Fe<sub>2</sub>O<sub>3</sub> or Fe<sup>3+</sup><sub>2</sub>O<sub>3</sub> (Alibert 2016). Cerium iron silicon deuteride, classified as a REE material within the lanthanide group, represents a significant REE presence in the samples (Dahle & Arai 2015). Notably, the XRD analysis showed the highest potential REE content in samples T1 and T7, with cerium iron silicon deuteride concentrations of 19.8% and 19.4%, respectively. These findings highlight the REE potential of the Sangiran sediments, particularly in regions represented by T1 and T7.

The SEM (Scanning Electron Microscope), combined with an X-ray EDS (Energy Dispersive Spectrometer), is a powerful analytical tool widely used for characterizing the morphology and chemical composition of materials at the microscale. By leveraging the interaction between an electron beam and the sample, SEM provides high-resolution imaging of surface topography, while EDS generates X-ray spectra that enable quantitative and qualitative analysis of the sample's elemental composition. This integrated technique is extensively applied across diverse fields, including materials science and geoscience, making it an indispensable instrument for advanced research and analysis.

The SEM analysis of the mud surface showed the presence of various minerals, including hematite (Fe<sub>2</sub>O<sub>3</sub>) and complex hybrid compounds containing cerium (Ce), iron (Fe), silicon (Si), and deuterium (D). These minerals exhibit significant porosity, with numerous pores between the grains and microcracks distributed across the mineral crystals. At a magnification of 650 times, cavities and hematite grains were observed to be evenly distributed across the sample surface, as shown in Figure 6. Hematite flakes and cerium iron silicon deuteride compounds were prominently visible, predominantly adhered to the quartz surfaces within the sample, as shown in Table 5.

SEM-EDS analysis of the SMV samples identified the presence of several elements, including C, O, Fe, Na, Mg, Al, Si, Cl, K, and Ca (Figure 7). Oxygen (O) was the most abundant element, with a weight percentage of 46.63%, followed by silicon (Si) at 17.24% and aluminum (Al) at 9.16%. These findings highlight the significant oxide content in the mud, supporting its role as a medium for the formation of REE. The SEM-EDS spectrum further showed that carbon (C) and oxygen (O) were the primary

constituents, while lower concentrations of Al, Si, Fe, K, and Ca were observed. Minor elements, including Mg and Na, were also detected in trace amounts.

Complementary ICP-OES analysis confirmed the presence of several REEs in the Sangiran mud samples, including Ce, Dy, Eu, Gd, Ho, La, Nd, Pr, Sm, Tb, Y, and Sc. However, the elements Lu, Yb, and Tm were below the detection limit. Quantitative analysis indicated that cerium (Ce) and lanthanum (La) were the most abundant REEs, with average concentrations of 37.96 ppm and 44.39 ppm, respectively. A detailed summary of the ICP-OES analysis results is provided in Table 6.

The concentration of REE in the Earth's crust ranges from  $130~\mu g/g$  to  $240~\mu g/g$ , surpassing the abundance of many other commonly exploited elements and significantly exceeding their respective chondritic abundances. Sangiran mud samples contain both light REE (LREE) and heavy REE (HREE), with detected elements including lanthanum (La), cerium (Ce), praseodymium (Pr), neodymium (Nd), and samarium (Sm). As presented in Table 5, the REE concentrations across samples T1 to T7 exhibit minimal variation, with differences in minimum and maximum concentrations ranging from 0.5 to 10 ppm. However, notable deviations are observed for cerium (Ce) and gadolinium (Gd), which display differences of 24 ppm and 18 ppm, respectively.

The variation in sample texture has a limited impact on REE concentrations. Dense mud samples, such as T1 and T4, tend to show lower Gd concentrations, typically below 10 ppm. In contrast, softer mud samples (T2, T3, T5, T6, and T7) exhibit higher Gd concentrations, ranging from 14 ppm to 20 ppm. Gadolinium oxide (GdO<sub>2</sub>) constitutes approximately 0.7% to 4.0% of the total REE content, with REEs accounting for only 4.0% of the mineral composition. This underscores the rarity of gadolinium within the analyzed samples.

Lutetium (Lu) in monazite minerals is typically present in trace amounts, with a concentration of approximately 0.003%. This aligns with the findings of this study, where Lu was not detected and could not be identified through ICP-OES analysis of Sangiran mud samples. Similarly, thulium (Tm) was also absent in the samples. Tm is not found in a free state but is associated with specific minerals such as monazite, gadolinite, xenotime, and euxenite. As one of the least abundant elements on Earth, its absence in Sangiran mud is consistent with its known scarcity.

The Lanthanum (La) exhibits the highest concentration among the REEs in Sangiran mud, with an average value of 44.39 ppm. Other detected REEs have concentrations ranging from 4.671 to 37.96 ppm. Notable elements include La (44.39 ppm) and cerium (Ce) (37.96 ppm), while the elements with the lowest concentrations are holmium (Ho) and yttrium (Y). Holmium is a minor component of minerals such as monazite and bastnaesite, often extracted during the processing of these minerals. Yttrium, another REE, is typically obtained through ion exchange and

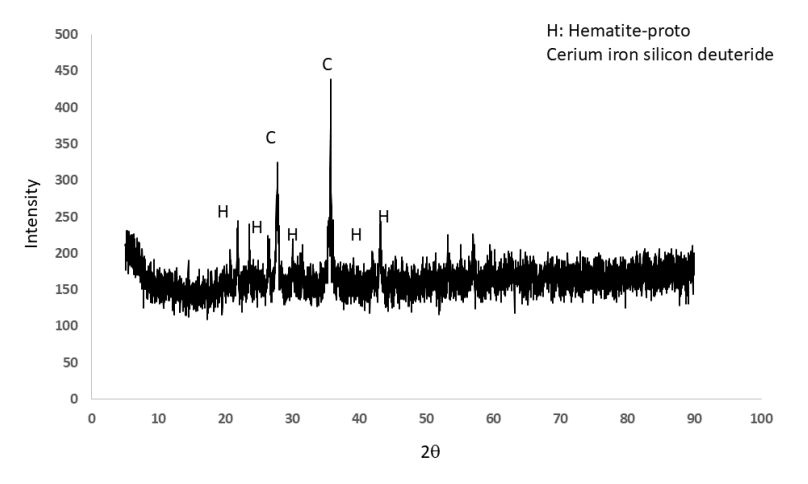


FIGURE 3. XRD characterization results of sample T1

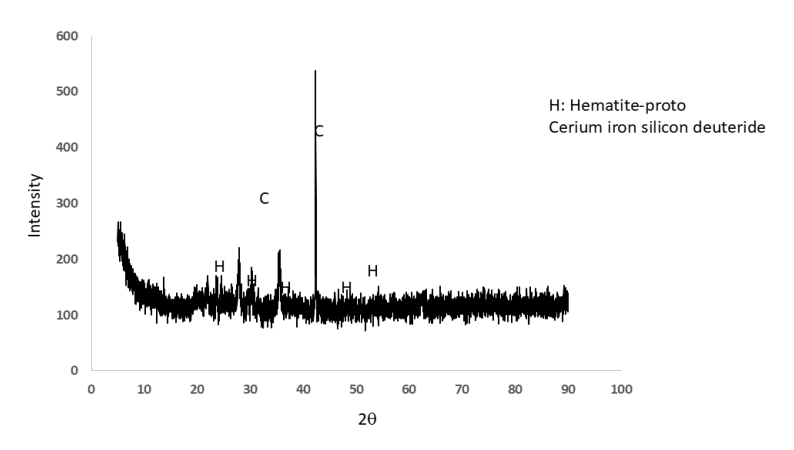


FIGURE 4. XRD characterization results of sample T4

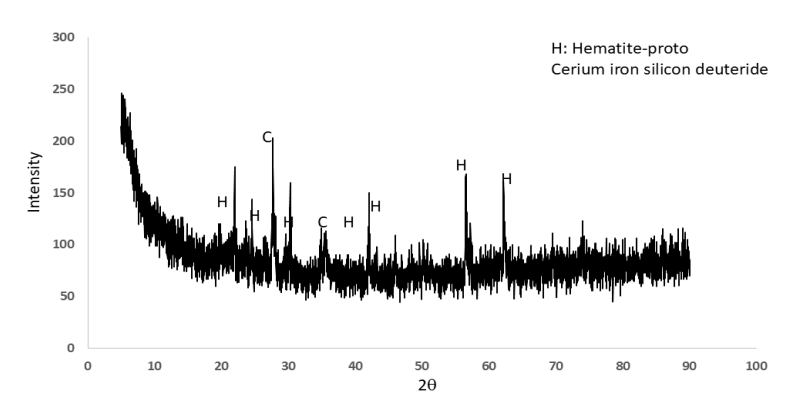


FIGURE 5. XRD characterization results of sample T7

TABLE 4. Compound concentration of the Sangiran mud samples

| Compound                      | T1 (%) | T4 (%) | T7 (%) | Min (%) | Max (%) | Mean (%) | Density (g/cm³) |
|-------------------------------|--------|--------|--------|---------|---------|----------|-----------------|
| Hematite-proto                | 80.2   | 88.7   | 80.6   | 80.2    | 88.7    | 83.17    | 5.283           |
| Cerium iron silicon Deuteride | 19.8   | 11.3   | 19.4   | 11.3    | 19.8    | 16.83    | 7.393           |

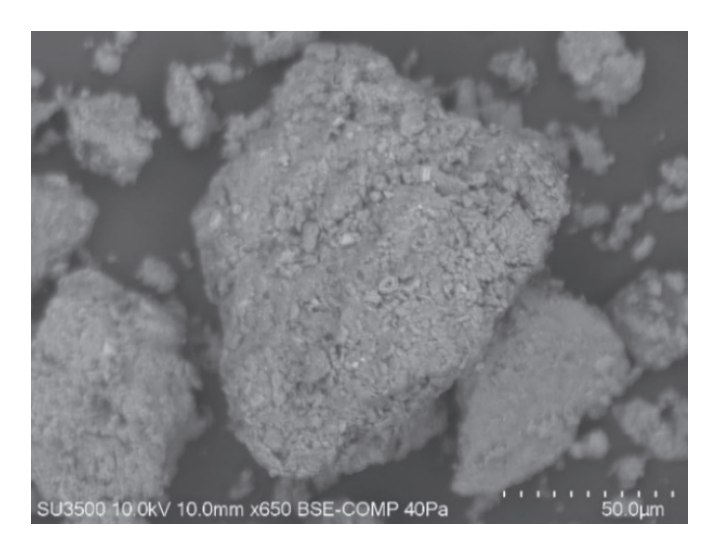


FIGURE 6. SEM-EDS image illustrating the SMV samples morphology

| TABLE 5. | Quantifying | the spectral | data |
|----------|-------------|--------------|------|
|----------|-------------|--------------|------|

| Elements | Weight (%) | Atomic (%) | Error (%) |
|----------|------------|------------|-----------|
| CK       | 21.07      | 30.35      | 9.21      |
| OK       | 46.63      | 50.44      | 7.18      |
| FeL      | 1.31       | 0.40       | 14.25     |
| NaK      | 0.42       | 0.32       | 16.88     |
| MgK      | 0.53       | 0.37       | 7.96      |
| AlK      | 9.16       | 5.88       | 3.78      |
| SiK      | 17.24      | 10.62      | 3.52      |
| ClK      | 0.32       | 0.16       | 17.33     |
| KK       | 1.47       | 0.65       | 10.26     |
| CaK      | 1.86       | 0.80       | 8.14      |

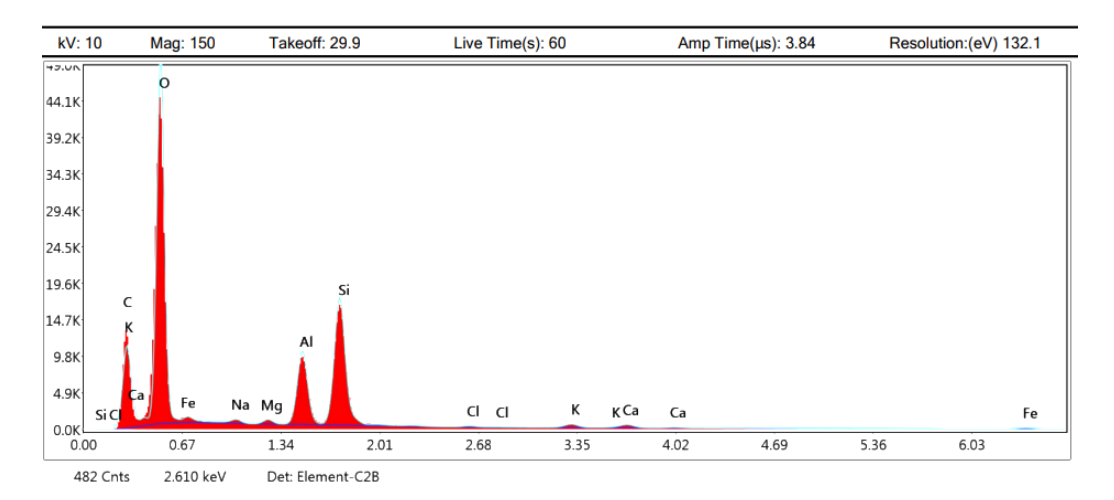


FIGURE 7. Corresponding EDS spectrum illustrating the elemental composition

| Elements |                                                                                                                                                                                                                                  | REE concentration (ppm)                                                                                                                                                                              |                                                                                                                                                                          |                                                                                                                                              |                                                                                                                  |                                                                                      |                                                          | Min. (ppm) | Max. (ppm) | Avg. (ppm) |
|----------|----------------------------------------------------------------------------------------------------------------------------------------------------------------------------------------------------------------------------------|------------------------------------------------------------------------------------------------------------------------------------------------------------------------------------------------------|--------------------------------------------------------------------------------------------------------------------------------------------------------------------------|----------------------------------------------------------------------------------------------------------------------------------------------|------------------------------------------------------------------------------------------------------------------|--------------------------------------------------------------------------------------|----------------------------------------------------------|------------|------------|------------|
|          | T1                                                                                                                                                                                                                               | T2                                                                                                                                                                                                   | Т3                                                                                                                                                                       | T4                                                                                                                                           | T5                                                                                                               | T6                                                                                   | T7                                                       |            |            |            |
| La       | 45.9                                                                                                                                                                                                                             | 52.2                                                                                                                                                                                                 | 41.8                                                                                                                                                                     | 42.5                                                                                                                                         | 41.4                                                                                                             | 44.6                                                                                 | 42.3                                                     | 41.4       | 52.2       | 44.39      |
| Ce       | 39.0                                                                                                                                                                                                                             | 55.8                                                                                                                                                                                                 | 33.2                                                                                                                                                                     | 36.9                                                                                                                                         | 33.1                                                                                                             | 36.0                                                                                 | 31.7                                                     | 31.7       | 55.8       | 37.96      |
| Pr       | 16.5                                                                                                                                                                                                                             | 26                                                                                                                                                                                                   | 22.2                                                                                                                                                                     | 20                                                                                                                                           | 23.0                                                                                                             | 22                                                                                   | 19.9                                                     | 16.5       | 26         | 21.37      |
| Nd       | 15.2                                                                                                                                                                                                                             | 21.4                                                                                                                                                                                                 | 18.7                                                                                                                                                                     | 18.7                                                                                                                                         | 19.4                                                                                                             | 18.7                                                                                 | 16.5                                                     | 15.2       | 21.4       | 18.37      |
| Tb       | 17.3                                                                                                                                                                                                                             | 16.6                                                                                                                                                                                                 | 16.6                                                                                                                                                                     | 16.5                                                                                                                                         | 16.5                                                                                                             | 16.5                                                                                 | 16.6                                                     | 16.5       | 17.3       | 16.66      |
| Sm       | 9.5                                                                                                                                                                                                                              | 17.6                                                                                                                                                                                                 | 14.8                                                                                                                                                                     | 14.9                                                                                                                                         | 16.2                                                                                                             | 13.9                                                                                 | 11.9                                                     | 9.5        | 17.6       | 14.11      |
| Gd       | 1.8                                                                                                                                                                                                                              | 14.2                                                                                                                                                                                                 | 18.0                                                                                                                                                                     | 7.3                                                                                                                                          | 17.3                                                                                                             | 20.1                                                                                 | 15.7                                                     | 1.8        | 20.1       | 13.49      |
| Dy       | 9.5                                                                                                                                                                                                                              | 10.6                                                                                                                                                                                                 | 12.7                                                                                                                                                                     | 10.8                                                                                                                                         | 12.6                                                                                                             | 13.6                                                                                 | 11.0                                                     | 9.5        | 13.6       | 11.54      |
| Sc       | 14.9                                                                                                                                                                                                                             | 11.5                                                                                                                                                                                                 | 9.9                                                                                                                                                                      | 9.9                                                                                                                                          | 8.7                                                                                                              | 11.8                                                                                 | 12.1                                                     | 8.7        | 14.9       | 11.26      |
| Eu       | 10.5                                                                                                                                                                                                                             | 10.4                                                                                                                                                                                                 | 10.1                                                                                                                                                                     | 10.1                                                                                                                                         | 10.0                                                                                                             | 10.2                                                                                 | 10.1                                                     | 10.0       | 10.5       | 10.20      |
| Y        | 5.9                                                                                                                                                                                                                              | 5.4                                                                                                                                                                                                  | 3.6                                                                                                                                                                      | 5.1                                                                                                                                          | 4.0                                                                                                              | 4.8                                                                                  | 3.9                                                      | 3.6        | 5.9        | 4.67       |
| Но       | <idl< td=""><td><idl< td=""><td>0.9</td><td>0.4</td><td>1.0</td><td><idl< td=""><td><idl< td=""><td>0.0</td><td>1.0</td><td>0.33</td></idl<></td></idl<></td></idl<></td></idl<>                                                 | <idl< td=""><td>0.9</td><td>0.4</td><td>1.0</td><td><idl< td=""><td><idl< td=""><td>0.0</td><td>1.0</td><td>0.33</td></idl<></td></idl<></td></idl<>                                                 | 0.9                                                                                                                                                                      | 0.4                                                                                                                                          | 1.0                                                                                                              | <idl< td=""><td><idl< td=""><td>0.0</td><td>1.0</td><td>0.33</td></idl<></td></idl<> | <idl< td=""><td>0.0</td><td>1.0</td><td>0.33</td></idl<> | 0.0        | 1.0        | 0.33       |
| Lu       | <idl< td=""><td><idl< td=""><td><idl< td=""><td><idl< td=""><td><idl< td=""><td><idl< td=""><td><idl< td=""><td>0.0</td><td>0.0</td><td>0.00</td></idl<></td></idl<></td></idl<></td></idl<></td></idl<></td></idl<></td></idl<> | <idl< td=""><td><idl< td=""><td><idl< td=""><td><idl< td=""><td><idl< td=""><td><idl< td=""><td>0.0</td><td>0.0</td><td>0.00</td></idl<></td></idl<></td></idl<></td></idl<></td></idl<></td></idl<> | <idl< td=""><td><idl< td=""><td><idl< td=""><td><idl< td=""><td><idl< td=""><td>0.0</td><td>0.0</td><td>0.00</td></idl<></td></idl<></td></idl<></td></idl<></td></idl<> | <idl< td=""><td><idl< td=""><td><idl< td=""><td><idl< td=""><td>0.0</td><td>0.0</td><td>0.00</td></idl<></td></idl<></td></idl<></td></idl<> | <idl< td=""><td><idl< td=""><td><idl< td=""><td>0.0</td><td>0.0</td><td>0.00</td></idl<></td></idl<></td></idl<> | <idl< td=""><td><idl< td=""><td>0.0</td><td>0.0</td><td>0.00</td></idl<></td></idl<> | <idl< td=""><td>0.0</td><td>0.0</td><td>0.00</td></idl<> | 0.0        | 0.0        | 0.00       |
| Tm       | <idl< td=""><td><idl< td=""><td><idl< td=""><td><idl< td=""><td><idl< td=""><td><idl< td=""><td><idl< td=""><td>0.0</td><td>0.0</td><td>0.00</td></idl<></td></idl<></td></idl<></td></idl<></td></idl<></td></idl<></td></idl<> | <idl< td=""><td><idl< td=""><td><idl< td=""><td><idl< td=""><td><idl< td=""><td><idl< td=""><td>0.0</td><td>0.0</td><td>0.00</td></idl<></td></idl<></td></idl<></td></idl<></td></idl<></td></idl<> | <idl< td=""><td><idl< td=""><td><idl< td=""><td><idl< td=""><td><idl< td=""><td>0.0</td><td>0.0</td><td>0.00</td></idl<></td></idl<></td></idl<></td></idl<></td></idl<> | <idl< td=""><td><idl< td=""><td><idl< td=""><td><idl< td=""><td>0.0</td><td>0.0</td><td>0.00</td></idl<></td></idl<></td></idl<></td></idl<> | <idl< td=""><td><idl< td=""><td><idl< td=""><td>0.0</td><td>0.0</td><td>0.00</td></idl<></td></idl<></td></idl<> | <idl< td=""><td><idl< td=""><td>0.0</td><td>0.0</td><td>0.00</td></idl<></td></idl<> | <idl< td=""><td>0.0</td><td>0.0</td><td>0.00</td></idl<> | 0.0        | 0.0        | 0.00       |
| Yb       | <idl< td=""><td><idl< td=""><td><idl< td=""><td><idl< td=""><td><idl< td=""><td><idl< td=""><td><idl< td=""><td>0.0</td><td>0.0</td><td>0.00</td></idl<></td></idl<></td></idl<></td></idl<></td></idl<></td></idl<></td></idl<> | <idl< td=""><td><idl< td=""><td><idl< td=""><td><idl< td=""><td><idl< td=""><td><idl< td=""><td>0.0</td><td>0.0</td><td>0.00</td></idl<></td></idl<></td></idl<></td></idl<></td></idl<></td></idl<> | <idl< td=""><td><idl< td=""><td><idl< td=""><td><idl< td=""><td><idl< td=""><td>0.0</td><td>0.0</td><td>0.00</td></idl<></td></idl<></td></idl<></td></idl<></td></idl<> | <idl< td=""><td><idl< td=""><td><idl< td=""><td><idl< td=""><td>0.0</td><td>0.0</td><td>0.00</td></idl<></td></idl<></td></idl<></td></idl<> | <idl< td=""><td><idl< td=""><td><idl< td=""><td>0.0</td><td>0.0</td><td>0.00</td></idl<></td></idl<></td></idl<> | <idl< td=""><td><idl< td=""><td>0.0</td><td>0.0</td><td>0.00</td></idl<></td></idl<> | <idl< td=""><td>0.0</td><td>0.0</td><td>0.00</td></idl<> | 0.0        | 0.0        | 0.00       |

TABLE 6. Rare Earth Element (REE) concentrations of the SMV samples

solvent extraction processes. Due to its ability to absorb neutrons, holmium is utilized in nuclear reactors to regulate chain reactions.

Geochemical analysis of the Sangiran mud samples confirms the presence of REEs, with 12 out of the 17 known REEs successfully identified. The formation and enrichment of REEs in the Sangiran mud are believed to be closely influenced by tectonic processes in the surrounding region. While REE availability is typically associated with volcanic activity, where elevated temperatures and pressures drive geochemical reactions that facilitate REE mobilization, the SMV, despite its distance from active volcanic centers, displays REE signatures likely linked to its association with subsurface hydrocarbon deposits.

Comparative analysis indicates that REE concentrations in Sangiran mud are lower than those found in the Lapindo mud volcano but are comparable to those in the Bledug Kuwu mud volcano. Both Sangiran and Bledug Kuwu are geographically isolated from modern volcanic systems, yet they exhibit REE presence due to their location within hydrocarbon-rich tectonic settings. In contrast, the Lapindo mud volcano is situated in East Java near Mount Penanggungan and also lies within an oil and gas reservoir zone, potentially benefiting from both magmatic and sedimentary contributions, thus resulting in higher REE concentrations.

Although the SMV shows no current volcanic activity, the detected REE content is hypothesized to originate from historical tectonic compression and deep crustal pressures that occurred millions of years ago. These processes may have facilitated the migration and concentration of REE-

bearing fluids. Despite its relatively modest REE levels compared to other sites, the SMV holds potential as a strategically valuable REE resource for Indonesia and warrants further exploration and evaluation.

The graph from Principal Component analysis visualizes that component one (PC1) has dominant compounds, namely SiO2, K2O, and ZrO2. Furthermore, component two (PC2) has dominant compounds, namely Fe<sub>2</sub>O<sub>3</sub>, Al<sub>2</sub>O<sub>3</sub>, and CaO, as shown in Figure 8. The test results of critical minerals using XRF and REE using ICP-OES were analyzed using Principal Component Analysis (PCA) to obtain the principal components (PCs) shown in Table 7. PC forms a new coordinate plane obtained from the maximum deviation of the initial data set and is a collection of dominant compounds or elements in a place. Table 7 shows the variation value of oxide compounds from PC1 by 56% and PC2 by 23% so that the cumulative variation value is 79%. The eigenvalues of PC1 and PC2 show values greater than 1, so each shows high representation. Based on the component plot of PCA in Figure 8, PC1 has dominant compounds namely Fe<sub>2</sub>O<sub>2</sub>, Al<sub>2</sub>O<sub>3</sub>, and CaO. While PC2 has dominant compounds namely SiO<sub>2</sub>, K<sub>2</sub>O, and CaO.

The position of oxide compounds that are close to each other on the graph indicates that these compounds have similar chemical properties in the analysis data. Conversely, oxides that are located far apart indicate a significant difference in chemical properties. On the graph, ZrO<sub>2</sub> and K<sub>2</sub>O are located close together on the positive side of PC1 and negative side of PC2, indicating that these two compounds tend to have complementary chemical properties in the formation of zirconium dioxide structures.

TABLE 7. Matrix values, eigen values, and yield variation values of oxide compounds

| Variable         | Component |        |  |  |  |
|------------------|-----------|--------|--|--|--|
| variable         | PC1       | PC2    |  |  |  |
| SiO <sub>2</sub> | 0.808     | 0.479  |  |  |  |
| $Fe_2O_3$        | -0.064    | 0.981  |  |  |  |
| $Al_2O_3$        | -0.257    | 0.004  |  |  |  |
| CaO              | -0.912    | -0.381 |  |  |  |
| $K_2O$           | 0.941     | -0.295 |  |  |  |
| $\mathrm{ZrO}_2$ | 0.945     | -0.130 |  |  |  |
| Eigen value      | 3.371     | 1.404  |  |  |  |
| Variation (%)    | 56.187    | 23.393 |  |  |  |

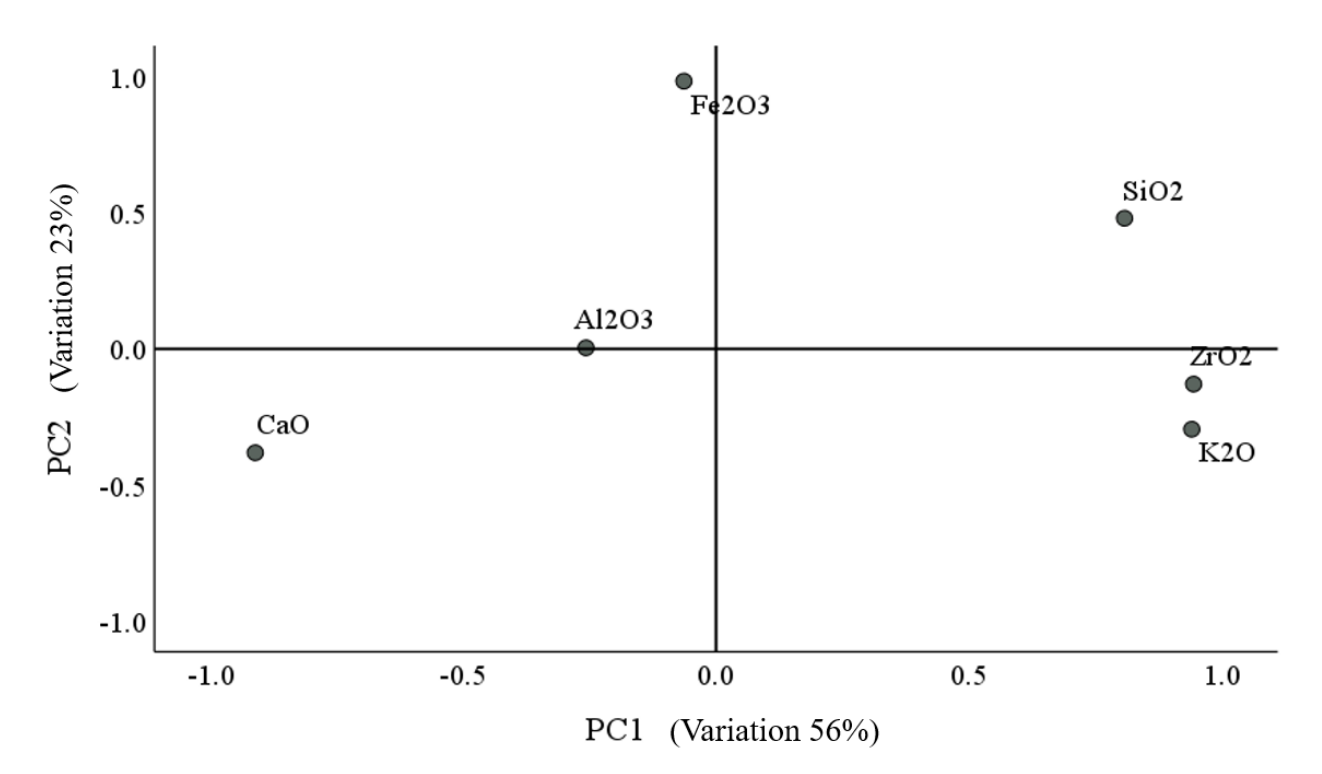


FIGURE 8. Distribution of oxide compound vs principal component

# CONCLUSIONS

Geochemical and mineralogical analyses of mud samples from the Sangiran Mud Volcano (SMV) show a composition predominantly characterized by hematite (Fe<sub>2</sub>O<sub>3</sub>; 83.16%) and cerium-bearing phases (16.83%). Hematite functions as the principal carrier of REEs, facilitating their incorporation through surface adsorption and structural substitution, while cerium phases suggest redox-controlled precipitation processes. Data obtained from XRF, XRD, and SEM-EDS analyses confirm the presence of major elements such as carbon (C), oxygen (O), silicon (Si), iron (Fe), calcium (Ca), and aluminium (Al), with REEs including Ce, Dy, Eu, Gd, Ho, La, Nd,

Pr, Sm, Tb, Y, and Sc. Lanthanum (La) and cerium (Ce) exhibited the highest concentrations, averaging 44.39 ppm and 37.96 ppm, respectively, while heavier REEs such as lutetium (Lu) and thulium (Tm) were not detected, likely due to their low natural abundance. Microscopic REE-bearing phosphates, particularly monazite, were observed within the hematite matrix, indicating localized REE mineralization. The dominance of SiO<sub>2</sub> and Fe<sub>2</sub>O<sub>3</sub>, alongside the identification of complex mineral assemblages such as cerium iron silicon deuterides and REE-fluorocarbonates (e.g., bastnäsite), reflects significant geochemical processes that facilitated REE enrichment, despite the absence of ongoing volcanic activity. These processes are

interpreted to result from the decomposition of volcanic glass and feldspar derived from past eruptions, which released REEs into hydrothermal fluids. High-temperature alteration and hydrothermal circulation, likely intensified by interactions with organic-rich, hydrocarbon-associated sediments, enhanced REE mobility through complexation with carboxylate ligands. Furthermore, the high Fe<sub>2</sub>O<sub>3</sub>/Al<sub>2</sub>O<sub>3</sub> ratios (>5) and textural variability among samples suggest that tectonic compression created fracture systems that acted as migration pathways for REE-enriched fluids. Collectively, these findings point to a complex interplay of tectonic, volcanic, and sedimentary processes that contributed to the anomalous REE concentrations in the Sangiran mud system.

#### ACKNOWLEDGEMENTS

This research was supported by funding from Universitas Negeri Malang through the Riset Kolaborasi Indonesia (RKI) grant, under contract number 17.5.44/UN32.20.1/LT/2022, for the 2022 fiscal year. Student author (Mariyanto) was funded through the Indonesian Education Scholarship (Beasiswa Pendidikan Indonesia or BPI) managed by Center for Higher Education Funding and Assessment (Pusat Pembiayaan dan Assesmen Pendidikan Tinggi or PPAPT), Ministry of Higher Education, Science, and Technology of the Republic of Indonesia (Kementerian Pendidikan Tinggi, Sains, dan Teknologi Republik Indonesia or Kemdiktisaintek RI) in collaboration with Indonesian Endowment Fund for Education (Lembaga Pengelola Dana Pendidikan or LPDP).

# REFERENCES

- Alibert, C. 2016. Rare earth elements in Hamersley BIF minerals. *Geochimica et Cosmochimica Acta* 184: 311-328. https://doi.org/10.1016/j.gca.2016.03.026
- Blengini, G.A., Nuss, P., Dewulf, J., Nita, V., Peirò, L.T., Vidal-Legaz, B., Latunussa, C., Mancini, L., Blagoeva, D., Pennington, D., Pellegrini, M., Van Maercke, A., Solar, S., Grohol, M. & Ciupagea, C. 2017. EU methodology for critical raw materials assessment: Policy needs and proposed solutions for incremental improvements. *Resources Policy* 53: 12-19. https://doi.org/10.1016/j.resourpol.2017.05.008
- Bronto, S., Asmoro, P. & Efendi, M. 2017. Gunung api lumpur di daerah Cengklik dan sekitarnya, Kabupaten Boyolali Provinsi Jawa Tengah. *Jurnal Geologi dan Sumberdaya Mineral* 18(3): 147-159. https://doi.org/10.33332/jgsm.geologi.v18i3.269
- Casadei, M., Ren, X., Rinke, P., Rubio, A. & Scheffler, M. 2012. Density-functional theory for *f*-electron systems: The α-γ phase transition in cerium. *Physical Review Letters* 109(14): 146402. https://doi.org/10.1103/PhysRevLett.109.146402

- Courtney-Davies, L., Ciobanu, C.L., Verdugo-Ihl, M.R., Dmitrijeva, M., Cook, N.J., Ehrig, K. & Wade, B.P. 2019. Hematite geochemistry and geochronology resolve genetic and temporal links among iron-oxide copper gold systems, Olympic Dam district, South Australia. *Precambrian Research* 335: 105480. https://doi.org/10.1016/j.precamres.2019.105480
- Dahle, J. & Arai, Y. 2015. Environmental geochemistry of cerium: Applications and toxicology of cerium oxide nanoparticles. *International Journal of Environmental Research and Public Health* 12(2): 1253-1278. https://doi.org/10.3390/ijerph120201253
- Dearing, J.A., Dann, R.J.L., Hay, K., Lees, J.A., Loveland, P.J., Maher, B.A. & O'Grady, K. 1996. Frequency-dependent susceptibility measurements of environmental materials. *Geophysical Journal International* 124(1): 228-240. https://doi.org/10.1111/j.1365-246X.1996.tb06366.x
- Dushyantha, N., Batapola, N., Ilankoon, I.M.S.K., Rohitha, S., Premasiri, R., Abeysinghe, B., Ratnayake, N. & Dissanayake, K. 2020. The story of rare earth elements (REEs): Occurrences, global distribution, genesis, geology, mineralogy and global production. *Ore Geology Reviews* 122: 103521. https://doi.org/10.1016/j.oregeorev.2020.103521
- El-Taher, A., Badawy, W.M., Khater, A.E.M. & Madkour, H.A. 2019. Distribution patterns of natural radionuclides and rare earth elements in marine sediments from the Red Sea, Egypt. *Applied Radiation and Isotopes* 151: 171-181. https://doi.org/10.1016/j.apradiso.2019.06.001
- Galos, K., Lewicka, E., Burkowicz, A., Guzik, K., Kot-Niewiadomska, A., Kamyk, J. & Szlugaj, J. 2021. Approach to identification and classification of the key, strategic and critical minerals important for the mineral security of Poland. *Resources Policy* 70: 101900. https://doi.org/10.1016/j.resourpol.2020.101900.
- Gwenzi, W., Mangori, L., Danha, C., Chaukura, N., Dunjana, N. & Sanganyado, E. 2018. Sources, behaviour, and environmental and human health risks of high-technology rare earth elements as emerging contaminants. *Science of The Total Environment* 636: 299-313. https://doi.org/10.1016/j.scitotenv.2018.04.235
- Hapsoro, C.A., Mariyanto, M., Agustine, E., Iryanti, M., Indriana, R.D., Rifai, M.K., Ibrahim, A. & Budiono, K.A. 2023. Identification of sediment formation based on magnetic content and element composition of mud volcano in Sangiran sediment using VSM and X-ray fluorescence. *JPSE (Journal of Physical Science and Engineering)* 8(1): 9. https://doi.org/10.17977/um024v8il2023p009

- Hidayat, W. & Novianto, A. 2020. Potential analysis of geological disasters 'mud volcano' at Boyolali and its surrounding areas based on geomagnetic methods. *AIP Conference Proceedings* 2251: 040006. https://doi.org/10.1063/5.0016349
- Indriana, R.D., Mariyanto, M., Agustin, E., Iryanti, M., Hapsoro, C.A., Koesuma, S. & Ashadi, A.L. 2024. Gravity interpretation of mud volcano based on satellite data (study case Kuwu and Cangkring Mud Volcano). *Indonesian Journal of Applied Physics* 14(1): 165. https://doi.org/10.13057/ijap. v14i1.84933
- Indriana, R.D., Saputra, H., Mariyanto, M., Agustin, E., Iryanti, M. & Hapsoro, C.A. 2023. Rare earth element characterization of Bledug Kuwu Mud Volcano, Central Java, Indonesia, based on geochemical analyzes (susceptibility, XRF, XRD, SEM-EDS and ICP-EOS). Sains Malaysiana 52(9): 2529-2543. https://doi.org/10.17576/jsm-2023-5209-05
- Isnaniawardhani, V., Muhamadsyah, F. & Sudrajat, A. 2018. Foraminifera assemblages as a marker of mud eruption source in Ciuyah, Ciniru Kuningan, West Java. *RISET Geologi dan Pertambangan* 28(2): 239. https://doi.org/10.14203/risetgeotam2018.v28.509
- Iwamori, H., Nakamura, H., Chang, Q., Morikawa, N. & Haraguchi, S. 2020. Multivariate statistical analyses of rare earth element compositions of spring waters from the Arima and Kii areas, Southwest Japan. *Geochemical Journal* 54(4): 165-182. https://doi.org/10.2343/geochemj.2.0583
- Kumar, V., Sharma, A., Kumar, R., Bhardwaj, R., Thukral, A.K. & Rodrigo-Comino, J. 2020. Assessment of heavy-metal pollution in three different Indian water bodies by combination of multivariate analysis and water pollution indices. *Human and Ecological Risk Assessment: An International Journal* 26(1): 1-16. https://doi.org/10.1080/10807039.2018.1497946
- Leventeli, Y. & Yalcin, F. 2021. Data analysis of heavy metal content in riverwater: Multivariate statistical analysis and inequality expressions. *Journal of Inequalities and Applications* 2021(1): 14. https://doi.org/10.1186/s13660-021-02549-3

- Maestrelli, D., Bonini, M. & Sani, F. 2019. Linking structures with the genesis and activity of mud volcanoes: Examples from Emilia and Marche (Northern Apennines, Italy). *International Journal of Earth Sciences* 108(5): 1683-1703. https://doi.org/10.1007/s00531-019-01730-w
- Mauri, G., Husein, A., Mazzini, A., Irawan, D., Sohrabi, R., Hadi, S., Prasetyo, H. & Miller, S.A. 2018a. Insights on the structure of Lusi mud edifice from land gravity data. *Marine and Petroleum Geology* 90: 104-115. https://doi.org/10.1016/j.marpetgeo.2017.05.041
- Mauri, G., Husein, A., Mazzini, A., Karyono, K., Obermann, A., Bertrand, G., Lupi, M., Prasetyo, H., Hadi, S. & Miller, S.A. 2018b. Constraints on density changes in the funnel-shaped caldera inferred from gravity monitoring of the Lusi mud eruption. *Marine* and Petroleum Geology 90: 91-103. https://doi. org/10.1016/j.marpetgeo.2017.06.030
- Mazzini, A. & Etiope, G. 2017. Mud volcanism: An updated review. *Earth-Science Reviews* 168: 81-112. https://doi.org/10.1016/j.earscirev.2017.03.001
- Mazzini, A., Sciarra, A., Lupi, M., Ascough, P., Akhmanov, G., Karyono, K. & Husein, A. 2023. Deep fluids migration and submarine emersion of the Kalang Anyar Mud Volcano (Java, Indonesia): A multidisciplinary study. *Marine and Petroleum Geology* 148: 105970. https://doi.org/10.1016/j.marpetgeo.2022.105970
- Novianto, Ardian, Sutanto, Suharsono, Prasetyadi, C. & W. Hidayat. 2022. Mud volcano: Revealing the stratigraphy of Kendeng Basin, Indonesia. *Open Journal of Yangtze Oil and Gas* 7(1): 48-64. https://doi.org/10.4236/ojogas.2022.71004
- Samankassou, Elias, Mazzini, A., Chiaradia, M., Spezzaferri, S., Moscariello, A. & Do Couto, D. 2018. Origin and age of carbonate clasts from the Lusi Eruption, Java, Indonesia. *Marine and Petroleum Geology* 90: 138-148. https://doi.org/10.1016/j.marpetgeo.2017.11.012
- \*Corresponding author; email: cahyo.ajihapsoro.fmipa@um.ac.id